

## Effect of thickness and surface composition on the stability of polarization in ferroelectric $\text{Hf}_x\text{Zr}_{1-x}\text{O}_2$ thin films

Adrian Acosta,<sup>1</sup> J. Mark P. Martinez ,<sup>1,2</sup> Norleakvisoth Lim,<sup>1</sup> Jane P. Chang ,<sup>1,\*</sup> and Emily A. Carter <sup>1,2,3,†</sup>

<sup>1</sup>*Department of Chemical and Biomolecular Engineering, University of California, Los Angeles, Los Angeles, California 90095, USA*

<sup>2</sup>*Princeton Plasma Physics Laboratory, Princeton, New Jersey 08540, USA*

<sup>3</sup>*Department of Mechanical and Aerospace Engineering and the Andlinger Center for Energy and the Environment, Princeton University, Princeton, New Jersey 08544-5263, USA*

 (Received 21 March 2022; revised 10 October 2023; accepted 2 November 2023; published 4 December 2023)

Using density functional theory, we find that tailoring the surface composition provides a route to stabilize the polar phases of the promising ferroelectric material,  $\text{Hf}_x\text{Zr}_{1-x}\text{O}_2$ . First, we show that for pure  $\text{HfO}_2$ , controlling the positively polarized surface to be relatively oxygen rich adequately screens the ferroelectric surface charges and stabilizes the polar orthorhombic phase. We then demonstrate that the ferroelectric polarization, as measured by the structural polar displacements, increases with decreasing thickness, leading to the emergence of a polar rhombohedral-like phase at the ultrathin limit (1.5 unit cells). Our findings extend to the cases of  $\text{Hf}_{0.5}\text{Zr}_{0.5}\text{O}_2$  and  $\text{ZrO}_2$ , both of which have surface energy landscapes similar to that of  $\text{HfO}_2$ . These findings are consistent with and offer insights into the observed absence of a ferroelectric thickness limit in  $\text{Hf}_x\text{Zr}_{1-x}\text{O}_2$ -based thin films.

DOI: [10.1103/PhysRevMaterials.7.124401](https://doi.org/10.1103/PhysRevMaterials.7.124401)

### I. INTRODUCTION

Over the last decade, the discovery of ferroelectric hafnia ( $\text{HfO}_2$ ) [1] has garnered great interest due to its intriguing and robust ferroelectricity at the nanoscale [2–5]. Its established compatibility with silicon semiconductor devices also makes  $\text{HfO}_2$ -based materials more promising for novel ferroelectric applications (e.g., ferroelectric memory and logic devices [6–9]) than perovskite oxides, which suffer from integration difficulties and chemical incompatibility with silicon [10–13]. Despite a plethora of studies on ferroelectric  $\text{HfO}_2$ , investigations to understand fully the factors that influence the stability of the polar phases (particularly the orthorhombic,  $Pca2_1$ ) versus nonpolar tetragonal ( $P4_2/nmc$ ) and monoclinic ( $P2_1/c$ ) phases are still ongoing [14–17].

Extensive prior work on perovskite ferroelectrics probed the influence of ferroelectric polarization on the stability of their surfaces, with several studies also pointing to the reciprocal effect: that one can tailor the structure of the interface or surface itself to stabilize the polarization strength or direction [18–22]. Here, we extend our prior work [23] characterizing the stability of ferroelectric  $\text{HfO}_2$  surfaces, in order to study this reverse effect: specifically, to determine whether the surface composition can be tailored to stabilize the ferroelectric polarization of  $\text{HfO}_2$  thin films.

Indeed, recent experiments have demonstrated that interfacial chemistry during deposition and crystallization of  $\text{HfO}_2$ -based thin films strongly influences their ferroelectric strength and performance [24–36]. We highlight in particular a recent study by Kelley *et al.* [37] that was able to

decouple the effect of the electrostatic potential and electrochemical surface states of  $\text{HfO}_2$  by controlling the external environment (oxygen partial pressure and temperature). Their observations using piezoresponse force microscopy confirmed that the stability of the ferroelectric phase is inseparable from the electrochemical state of the surface of  $\text{HfO}_2$ .

In terms of theoretical efforts to gain insight into the ferroelectric stability of  $\text{HfO}_2$  thin films, Batra *et al.* [38] used density functional theory (DFT) with the Perdew-Burke-Ernzerhof (PBE) exchange-correlation (XC) functional to study the stability of ferroelectric phases in stoichiometric O-terminated  $\text{HfO}_2$  slabs at small dimensions relative to nonpolar phases, based on their surface energies. They noted, however, that some models required the middle layers to be fixed during ionic relaxation to avoid phase transformations. Similarly, DFT-PBE simulations by Lee *et al.* [3] suggested ferroelectric polarization would remain stable in  $\sim$ one-unit-cell-thick Hf-terminated  $\text{HfO}_2$  slabs. However, their model fixed the Hf atoms to their bulk orthorhombic positions during ionic relaxation. Here, we show that the approximations made in these prior studies should not be assumed; these authors also did not explore whether the surface termination influences the stability of the bulklike ferroelectric polarization of freestanding  $\text{HfO}_2$  slabs. Since the surface or interface plays an outsized role in the stability of ferroelectric polarization at small dimensions, here we also seek to understand the influence of the thickness of  $\text{HfO}_2$  thin films on the stability of its ferroelectric polarization.

$\text{Hf}_x\text{Zr}_{1-x}\text{O}_2$  also exhibits ferroelectricity at reduced dimensions. In general, the polar orthorhombic phase of  $\text{Hf}_{0.5}\text{Zr}_{0.5}\text{O}_2$  thin films (particularly at a 1:1 ratio of Hf:Zr) is experimentally easier to stabilize than that phase of polar  $\text{HfO}_2$ , e.g., under a wider range of conditions or without need for additional dopants [17,39–43]. Additionally,

\*jpchang@ucla.edu

†eac@princeton.edu

ferroelectricity also has been reported to emerge at ultrathin thicknesses in  $\text{ZrO}_2$  thin films [44]. Thus, given the structural similarities of the fluorite  $\text{Hf}_{0.5}\text{Zr}_{0.5}\text{O}_2$  and  $\text{ZrO}_2$  to that of  $\text{HfO}_2$ , we also explore the influence of the surface composition and thickness effects in  $\text{Hf}_{0.5}\text{Zr}_{0.5}\text{O}_2$  and  $\text{ZrO}_2$ .

Christensen and Carter used DFT within the local density approximation to characterize the surfaces of tetragonal and monoclinic phases of  $\text{ZrO}_2$  [45]. The authors found the (111) and ( $\bar{1}11$ ) surfaces to be the most stable for the tetragonal and monoclinic phases, respectively, leading to an explanation of observed phase transitions at the nanoscale being driven by relative surface energies. Not surprisingly, the most stable surfaces exhibited stoichiometric numbers of Zr and O, i.e., 1:2, as they achieve the best electrostatic stability. The authors, however, did not consider the polar orthorhombic phase. While other studies have looked at the influence of various factors (e.g., strain, oxygen vacancies, and surface energy [46–48]) on the bulk polar phases of  $\text{ZrO}_2$ , those studies did not examine the effect of surface composition on the surface energy as a means to stabilize its ferroelectric polarization, as we do here.

## II. METHODS

To model the nature of  $\text{HfO}_2$ ,  $\text{Hf}_{0.5}\text{Zr}_{0.5}\text{O}_2$ , and  $\text{ZrO}_2$  thin films, we carried out spin-polarized DFT calculations under periodic boundary conditions using the Vienna *Ab initio* Simulation Package (VASP) version 5.4.4 [49]. We employed the PBE XC [50] generalized gradient approximation functional and the all-electron, frozen-core, projector augmented-wave (PAW) formalism, with the standard VASP PAW projectors accounting for electron-ion interactions, treating the  $2s$  and  $2p$  valence electrons for O; the  $5s$ ,  $5p$ ,  $6s$ , and  $5d$  outer core and valence electrons for Hf; and the  $4s$ ,  $4p$ ,  $5s$ , and  $4d$  outer core and valence electrons for Zr self-consistently [51]. We used Monkhorst-Pack meshes [52] for  $k$ -point sampling of the Brillouin zone and a kinetic energy (KE) cutoff of 800 eV for the plane wave (PW) basis expansion of the (smooth pseudo-) wave functions, which corresponds to ( $2^2 \times 800 \text{ eV} =$ ) 3200 eV and ( $1.5^2 \times 800 \text{ eV} =$ ) 1800 eV to represent the (smooth) electron densities of the bulk phases and slabs, respectively (the number of fast Fourier transform (FFT) grid points along each direction increased by 2.0 and 1.5 times, respectively). Because all the above-mentioned compounds are wide-band-gap semiconductors (insulators), we used Gaussian electronic smearing with a width of 0.01 eV to aid in electronic convergence.

We maintained the bulk optimized lattice vectors of  $\text{HfO}_2$  (determined in a prior work [23]),  $\text{Hf}_{0.5}\text{Zr}_{0.5}\text{O}_2$ , and  $\text{ZrO}_2$  (the latter two optimized in this work) for the in-plane vectors when constructing the surfaces (*vide infra*). The optimized lattice parameters for bulk orthorhombic  $\text{HfO}_2$  are  $a = 5.27 \text{ \AA}$ ,  $b = 5.06 \text{ \AA}$ ,  $c = 5.09 \text{ \AA}$ ; for  $\text{Hf}_{0.5}\text{Zr}_{0.5}\text{O}_2$  they are  $a = 5.29 \text{ \AA}$ ,  $b = 5.07 \text{ \AA}$ ,  $c = 5.10 \text{ \AA}$ ; and for  $\text{ZrO}_2$ , they are  $a = 5.32 \text{ \AA}$ ,  $b = 5.10 \text{ \AA}$ ,  $c = 5.13 \text{ \AA}$ , with  $\alpha = \beta = \gamma = 90.0^\circ$  for all compositions (see Table S1 in the Supplemental Material (SM) [53] (also see Refs. [35,54,55]) for a summary of the calculated lattice parameters, which are compared to experiment and the PBEsol XC functional [56]). The bulk orthorhombic structures of  $\text{Hf}_{0.5}\text{Zr}_{0.5}\text{O}_2$  and  $\text{ZrO}_2$  were initially

constructed by incrementally replacing Hf with Zr in the four-formula-unit bulk orthorhombic structure of  $\text{HfO}_2$  optimized in our prior work [23]. We used a  $4 \times 4 \times 4$   $k$ -point mesh for the bulk  $\text{Hf}_{0.5}\text{Zr}_{0.5}\text{O}_2$  and  $\text{ZrO}_2$  models. With these settings of PW KE cutoff and  $k$ -point sampling, the total energies were converged to within 1 meV/atom. For the bulk lattice-vector and atomic-coordinate optimization, we relaxed all atoms until the absolute atomic force components decreased to  $<0.001 \text{ eV/\AA}$ .

We modeled orthorhombic ( $Pca2_1$ )  $\text{HfO}_2(001)$ ,  $\text{Hf}_{0.5}\text{Zr}_{0.5}\text{O}_2(001)$ , and  $\text{ZrO}_2(001)$  thin films with thicknesses ranging from three to 11 layers (*vide infra*) constructed from the bulk orthorhombic structure with their polarization parallel to the surface normal. Except for the outermost surface layers (the composition of which we vary), each layer in the supercell models consist of two half layers: for the case of  $\text{HfO}_2$ , the half layers consist of either two Hf atoms or four O atoms; for the case of  $\text{Hf}_{0.5}\text{Zr}_{0.5}\text{O}_2$ , the half layers consist of either one Hf and one Zr atom or four O atoms; for the case of  $\text{ZrO}_2$ , the half layers consist of either two Zr atoms or four O atoms. This ordering produces an alternating positive (cationic) and negative (anionic) stacking pattern along the surface normal. As alluded to above, the supercell slab surfaces of  $\text{HfO}_2$ ,  $\text{Hf}_{0.5}\text{Zr}_{0.5}\text{O}_2(001)$ , and  $\text{ZrO}_2$  have in-plane lattice vectors corresponding to the optimized  $a$  and  $b$  lattice vectors of their respective bulk orthorhombic cells. We introduced an initial vacuum width of  $15 \text{ \AA}$  along the surface normal. We used a  $4 \times 4 \times 1$   $k$ -point mesh for the supercell slabs.

For all the slab structure optimizations, we kept the in-plane lattice vectors of the cell fixed to their equilibrium bulk values. We then allowed all atoms to relax freely in all directions until the absolute atomic force components on each decreased to  $<0.01 \text{ eV/\AA}$ . Only when evaluating the surface energy of the different compositions for a given bulk phase did we fix the middle five half layers during relaxation of the supercell slabs, in order to simulate a bulklike interior boundary condition for the surfaces and prevent phase transformation. We introduced dipole corrections (both energy and potential) to eliminate spurious interactions between periodic images across the vacuum space. For the energy convergence quality of the chosen computational parameters, please refer to Ref. [23]. To generate the figures in this paper, we used VESTA to visualize crystal structures and VASPKIT to calculate the plane-averaged electrostatic potential and electron density profiles [57,58].

## III. RESULTS

### A. Influence of the surface composition on polarization in pure $\text{HfO}_2$

Before examining how thickness affects the stability of polarization in orthorhombic  $\text{Hf}_x\text{Zr}_{1-x}\text{O}_2$  thin films, we first established the polarization response to the surface composition, beginning with pure  $\text{HfO}_2$  using an 11-Hf-half-layer thick slab. We compared the stability of the out-of-plane displacements within the slab for two surface compositions on the polar supercell slab structure of  $\text{HfO}_2$ : (1) a stoichiometric slab with O-terminated surfaces and symmetric compositions

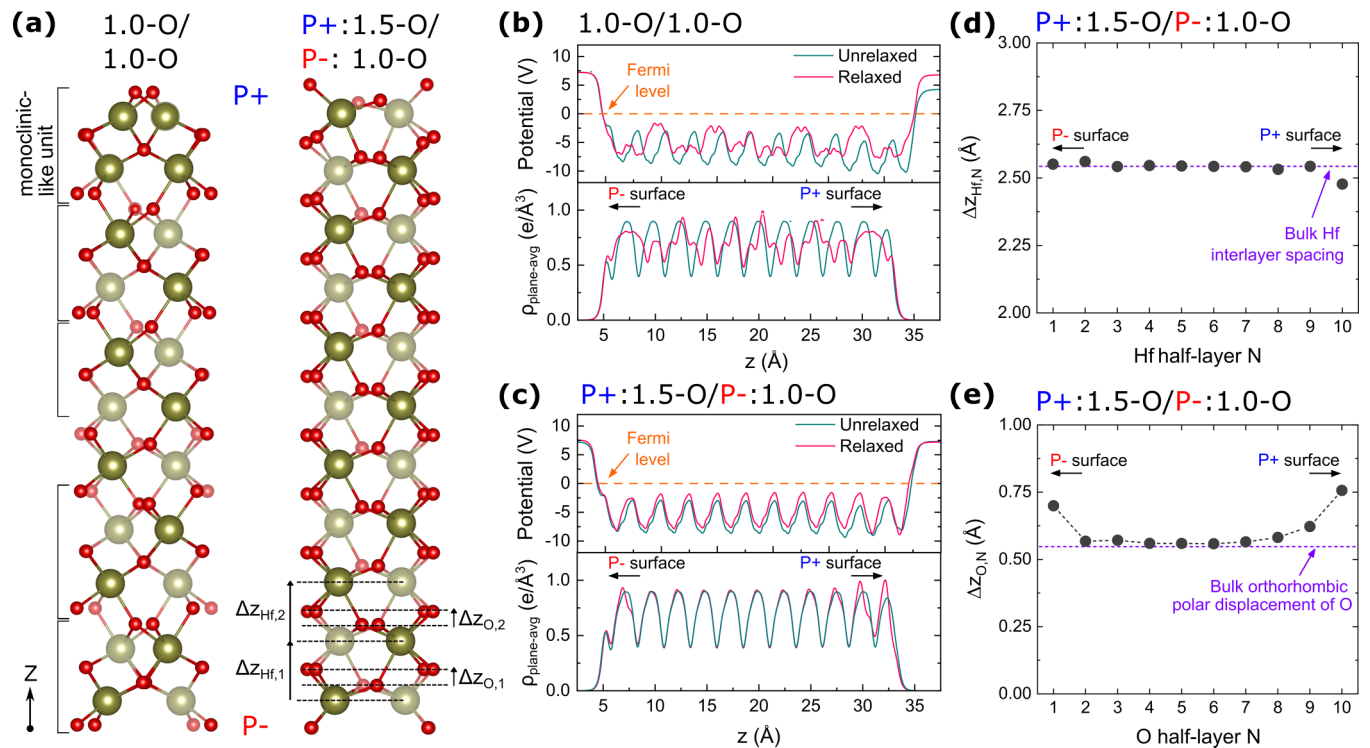


FIG. 1. (a) Profile views (after ionic relaxation) of the 11-Hf-half-layer-thick  $\text{HfO}_2$  supercell slabs constructed with symmetric (1.0-O/1.0-O) or asymmetric ( $\text{P}^+:\text{1.5-O}/\text{P}^-:\text{1.0-O}$ ) surface terminations. Green spheres are Hf; red spheres are O. Plane-averaged electrostatic potential (top panel) and plane-averaged electron density ( $\rho_{\text{plane-avg}}$ , bottom panel) are shown for (b) symmetrically and (c) asymmetrically terminated slabs along the direction of the surface normal, before and after ionic relaxation. The  $z$  coordinate starts from the middle of the vacuum (set to  $z = 0 \text{ \AA}$ ) through the oxide from the  $\text{P}^-$  surface [ $z \sim 5 \text{ \AA}$ , bottom of slabs in (a)] to the  $\text{P}^+$  surface [ $z \sim 33 \text{ \AA}$ , top of slabs in (a)] and back to the middle of the vacuum ( $z = 43.52 \text{ \AA}$ ). The plane-averaged potentials and electron densities ( $\rho_{\text{plane-avg}}$ ) are plotted from  $z = 2.5$  to  $37.5 \text{ \AA}$  to ensure small details remain visible in the composite figure. The potentials in the top panels are referenced to the Fermi level (set to 0), depicted with the dashed horizontal orange line. (d) Interlayer spacing from one Hf half layer to the next for asymmetrically terminated slabs along the direction of the surface normal. The  $N$ th Hf half layer begins at the  $\text{P}^-$  surface and ends at the  $\text{P}^+$  surface [as labeled in (a)]. Dashed purple line shows the bulk value for reference. (e) Intralayer spacing between O planes within each O half layer for asymmetrically terminated slabs along the direction of the surface normal. Each O half layer partitions into two O planes of two O atoms each and we use the distance of the average  $z$  coordinate of the two O in each plane. Illustration of the measure for this displacement is shown via dashed lines for  $N = 1$  and  $N = 2$  in (a). The  $N$ th O half layer begins at the  $\text{P}^-$  surface and ends at the  $\text{P}^+$  surface [as labeled in (a)]. Dashed purple line shows the bulk value for reference.

across the positive ( $\text{P}^+$ ) and negative ( $\text{P}^-$ ) polarized surfaces, and (2) a nonstoichiometric slab with asymmetric composition across the  $\text{P}^+$  and  $\text{P}^-$  surfaces. The choice of these two surface compositions stems from our prior work systematically evaluating various possible O and Hf coverages and terminations of nonpolar tetragonal and polar orthorhombic  $\text{HfO}_2$  surfaces [23]. Therein we found that although a compositionally symmetric surface (with outer layers consisting of one oxygen atom per surface formula unit on both surfaces, denoted 1.0-O/1.0-O) is the most stable for a nonpolar tetragonal slab, the same composition is unstable for a polar orthorhombic slab [23]. For the latter, an asymmetric termination of 1.5-O and 1.0-O per surface formula unit on the  $\text{P}^+$  and  $\text{P}^-$  surface, respectively (denoted  $\text{P}^+:\text{1.5-O}/\text{P}^-:\text{1.0-O}$ ), is more stable above 680 K for an  $\text{O}_2$  pressure of 1 bar. We showed that the greater stability of the latter arises from its ability to screen the surface polarization charges more effectively [23]. We illustrate in further detail the structures of these surfaces and the corresponding nomenclature used throughout the text in Fig. S1 in the SM [53]. Thus, given the

intimate relationship between ferroelectric polarization and surface stability, these two compositions provide contrasting cases to study the influence of the surface composition on ferroelectric stability. We will show later in this work that the surface energy landscape found in this prior study on pure  $\text{HfO}_2$  also extends to  $\text{Hf}_{0.5}\text{Zr}_{0.5}\text{O}_2$  and  $\text{ZrO}_2$ .

After full ionic relaxation with no fixed inner layers, the stoichiometric slab with symmetric surface composition 1.0-O/1.0-O (initialized with a bulk polar orthorhombic structure) transitions to a monoclinic phase [Fig. 1(a), left] which is nonpolar in its bulk ground state [39,59]. Figure 1(a), left, highlights the repeating four  $\text{HfO}_2$  formula units resembling a conventional monoclinic unit cell with its [001] axis normal to the surface. We include a profile view of the slabs in Fig. 1(a) with a depth perspective that also shows the vacuum within the supercell boundary in Fig. S1 of the SM [53]. For a comparison of the structural similarity, Fig. S2(a) in the SM presents two views of the optimized bulk monoclinic phase while Fig. S2(b) in the SM displays related views of the relaxed symmetric slab. Additionally, we compare the

interlayer Hf and intralayer O spacings for the bulk monoclinic and orthorhombic phases versus the symmetric  $\text{HfO}_2$  slab in Fig. S2(c) in the SM [53]. Note that because the 11-Hf-half-layer-thick slab contains 5.5 formula units of the conventional monoclinic unit cell, the center of the slab accommodates the remaining layer (0.5 formula units out of plane) to one that retains resemblance to the higher symmetry orthorhombic unit cell, which in turn contributes a residual polarization that we discuss later.

Ionic relaxation to a nonpolar monocliniclike phase is a consequence of the otherwise unscreened dipole of the polar orthorhombic phase. This depolarization manifests in the plane-averaged electrostatic potential and plane-averaged electron density ( $\rho_{\text{plane-avg}}$ ) plotted along the direction normal to the slab in Fig. 1(b). Before ionic relaxation, an electrostatic potential builds up across the slab and results in a net difference in electrostatic potential between the P− and P+ surfaces of 3.01 V. Ionic relaxation does not eliminate entirely but reduces this electrostatic potential difference to 0.46 V. Layer-by-layer projected densities of states (pDOS) in Fig. S3 in the SM [53] presents additional evidence of the necessity of ionic relaxation to avoid dielectric breakdown due to the initially unscreened electrostatic potential. Furthermore, note the asymmetric accumulation of electron density at the P+ surface compared to the P− surface before ionic relaxation [Fig. 1(b)]. This is a result of the need to screen the ferroelectric polarization in the absence of other charge compensating mechanisms. The charge balances more evenly between surfaces after ionic relaxation.

In contrast to the stoichiometric  $\text{HfO}_2$  slab with symmetrically terminated surfaces, the nonstoichiometric  $\text{HfO}_2$  slab with asymmetric surface composition maintains a bulk-like orthorhombic phase after ionic relaxation [Fig. 1(a), right]. Figure S2(d) provides additional viewing angles of the slab to visually compare with the bulk orthorhombic phase (Fig. S2(e) [53]). The ionic charge from additional O on the P+ surface compared to the stoichiometric symmetric  $\text{HfO}_2$  slab appears to provide sufficient charge screening needed to sustain polarization.

As further evidence of the stable ferroelectric polarization in the asymmetric  $\text{HfO}_2$  slab, note that before ionic relaxation (initialized with a bulk orthorhombic structure), the net electrostatic potential difference between the P− and P+ surfaces is only  $-0.09$  V [Fig. 1(c), top panel]. A perfectly screened polarization would have zero difference in the electrostatic potential between surfaces, but a slightly negative value arises from the excess O concentration at the P+ surface. After ionic relaxation, the net electrostatic potential reverses and its magnitude increases to 0.35 V. Later, we will show that thinner  $\text{HfO}_2$  slabs can sustain a stronger polarization than the bulk orthorhombic phase. Lastly, unlike the symmetric  $\text{HfO}_2$  slab, we observe in the bottom panel of Fig. 1(c) that the excess electron density that accumulates near the P+ surface does not redistribute toward the P− surface after ionic relaxation and in fact grows.

To show how the orthorhombic phase persists across the entire asymmetric  $\text{HfO}_2$  slab, we plot in Fig. 1(d) the interlayer spacings between each Hf half layer to the next, starting at the P− surface and moving toward the P+ surface. The spacings remain close to the bulk orthorhombic value of

2.54 Å. The asymmetric profile of the Hf spacings between the top and bottom surfaces stems from the difference in the composition of the two surfaces. Of note, the inward relaxation of the Hf atoms on the P+ surface ( $\sim 2.7\%$  relative to the bulk) likely serves to reduce the positive polarization charge on this surface. Additionally, to compare the polarization of the supercell slabs to the bulk polarization, we plotted in Fig. 1(e) the intralayer displacement between the two planes of O atoms within each O half layer, along the surface-normal coordinate. The polar displacements near the center lie close to the bulk value (0.55 Å) with larger deviations occurring toward the surface (an indication of enhanced polarization near the surface).

### B. Influence of the thickness on polarization in pure $\text{HfO}_2$

Given that only the thick slab with asymmetric termination supports permanent polarization, we focus on this composition henceforth. We therefore next explore the influence of thickness on the ferroelectric stability of asymmetrically terminated (P+:1.5-O/P−:1.0-O) orthorhombic  $\text{HfO}_2$  slabs by constructing additional models with nine, seven, five, and three Hf half layers. The displacements near the center resemble the bulk polar displacement O with larger deviations occurring near the surface. Figure 2(a) plots the average values of the polar displacements across the asymmetric slabs, which increase from  $\sim 10.3\%$  to  $\sim 26.3\%$  larger than the bulk going from an 11-Hf-half-layer thickness down to a five-Hf-half-layer thickness (Fig. S4 [53] shows the layer-by-layer displacements for all thicknesses). Conversely, we expect that as the slab thickness increases, this value will approach the bulk limit. Similar behavior of increasing polarization in  $\text{HfO}_2$ -based thin films with decreasing thickness has been observed—e.g., by Cheema *et al.* in  $\text{Hf}_{0.8}\text{Zr}_{0.2}\text{O}_2$  and Lyu *et al.* in  $\text{Hf}_{0.5}\text{Zr}_{0.5}\text{O}_2$  thin films [2,4].

We omitted a comparison for the asymmetric three-Hf-half-layer-thick slab from Fig. 2(a) because the structure undergoes a phase transition that no longer resembles the orthorhombic phase [see Fig. 2(c), bottom] and the characteristic intralayer polar displacements of O in the orthorhombic phase no longer apply. However, the symmetric three-Hf-half-layer-thick slab retains a strong bulklike polarization with an average polar displacement of  $\sim 40.5\%$  larger than the bulk. We discuss these special cases for both the symmetric and asymmetric three-Hf-half-layer-thick slabs further below.

To gain further insight into the stability of polarization, we plot in Fig. 2(b) the net electrostatic potential of the  $\text{HfO}_2$  slabs before and after ionic relaxation for varying thicknesses, calculated by subtracting the electrostatic potential in the vacuum near the P+ surface from that of the P− surface. Figure S5 in the SM displays the full electrostatic potential profiles [53]. The 1.0-O/1.0-O-terminated  $\text{HfO}_2$  slabs (at five- to 11-Hf-half-layer thickness) undergo ionic relaxation that depolarizes the structure to eliminate the otherwise strong, unscreened electrostatic potential [Fig. 2(b), open squares]. Note that a residual polarization exists for all the symmetric slabs, even after relaxation. For the five- to 11-layer slabs with an odd number of Hf half layers, we attribute this to the fact that a residual single layer of the polar orthorhombic phase is accommodated in the center of the slab instead of half of a

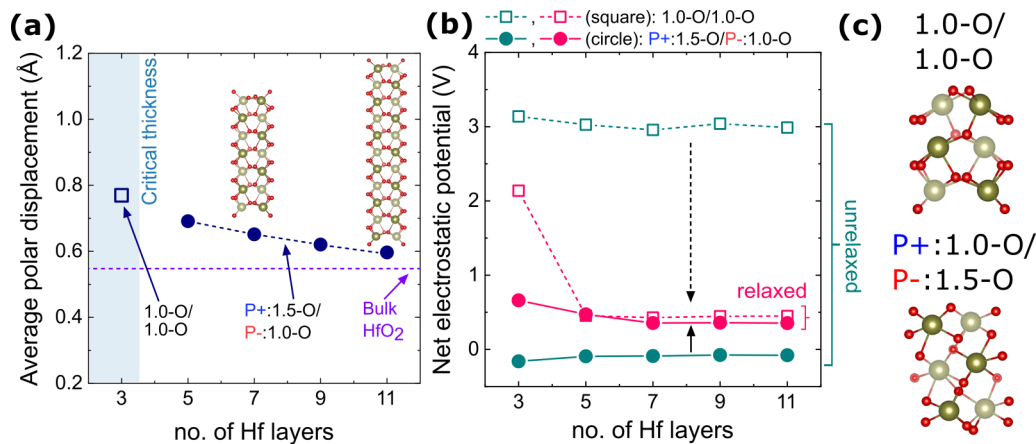


FIG. 2. (a) Average value of the polar displacements of O [as defined in Fig. 1(a)] for asymmetrically terminated orthorhombic  $\text{HfO}_2$  slabs with varying thickness (the layer-by-layer displacement profiles, as was plotted for the case of 11 Hf half layers in Fig. 1(c), are shown in Fig. S4 in the SM [53]). Inset figures show the 11- and seven-Hf-half-layer-thick slabs (green spheres are Hf; red spheres are O) and the dashed purple line provides a comparison to the bulk polar displacement. At three Hf layers (labeled “critical thickness”) the asymmetric  $\text{HfO}_2$  structure [shown in bottom panel (c)] deviates significantly from the bulk orthorhombic phase. Consequently, we do not plot its average O displacement. In its place, we plot the average polar displacement for the symmetric slab [top panel (c)]. (b) Net electrostatic potential as a function of total slab thickness for symmetrically and asymmetrically terminated orthorhombic  $\text{HfO}_2$  slabs, before (dark cyan) and after (pink) ionic relaxation. (c) Optimized structures for the symmetric (top panel) and asymmetric (bottom panel)  $\text{HfO}_2$  slabs at a thickness of three Hf half layers.

monocliniclike unit cell after relaxation [e.g., see Fig. 1(b)]. By contrast, for a four-Hf-half-layer-thick slab (which has the same number of atoms in a monoclinic unit cell), the electrostatic potential drop between the two surfaces reaches  $\sim 0$  V after relaxation (not shown).

Even before relaxation, all the asymmetric P+:1.5-O/P-:1.0-O-terminated  $\text{HfO}_2$  slabs maintain only a small net electrostatic potential due to the successful screening of the polarization via a nonstoichiometric construction [Fig. 2(b), filled dark cyan circles]. With fewer layers, the accumulated dipole moment and associated net electrostatic potential from the ionically screened ferroelectric displacements in each layer becomes more negative. As a result, prior to relaxation, the magnitude of the net electrostatic potential strengthens from  $-0.07$  to  $-0.16$  V going from 11- to three-Hf-half-layer thickness. After relaxation, the direction of the polarization reverses, and as in the unrelaxed case, the slabs retain an increasingly stronger unscreened net electrostatic potential with decreasing thickness (although opposite in direction).

We next examine the behavior of symmetric and asymmetric  $\text{HfO}_2$  slabs at a three-Hf-half-layer thickness [Fig. 2(c) displays the profiles]. At this critical thickness, a symmetric  $\text{HfO}_2$  slab retains an orthorhombic bulklike phase after ionic relaxation while supporting a strong, unscreened net electrostatic potential [2.14 V, Fig. 2(b)], in contrast to thicker symmetric slabs. An unscreened stable ferroelectric polarization can in principle be stable without the need for compensating surface charges to avoid electrostatic divergence, as long as the electrostatic potential energy is smaller than the band gap to avoid dielectric breakdown. This has been predicted to be the case for polar binary oxides below a critical thickness of several layers [60,61]. Thus, despite the presence of the unscreened electrostatic potential, the symmetric three Hf half layer thick slab has a calculated band gap of  $\sim 2.0$  eV (Fig. S6(b) [53]) and remains insulating throughout

its thickness. Note that the lowering of the band gap compared to the bulk orthorhombic  $\text{HfO}_2$  phase ( $\sim 4.3$  eV [23]) as the slab becomes thinner is due to increased covalency and polarization (leading to stronger band bending) near and at the surface, which consequently eases charge transfer between the valence and conduction of bands of the P- and P+ outermost layers, respectively, further enhancing charge screening. Despite the reduction in band gap, it remains relatively large. Note also that our DFT bulk value [23] is lower than the measured values (5.25–5.95 eV) from x-ray photoelectron spectroscopy and spectroscopic ellipsometry for thin films, as also expected [62–65].

Furthermore, we find that the asymmetric three Hf half layer thick  $\text{HfO}_2$  slab remains polar [Fig. 2(b)] but undergoes a structural phase change that is accompanied by a change in composition at the top (P+) of the slab from 1.5-O to 1.0-O (3-O to 2-O per unit cell) and vice versa for the bottom (P-) of the slab. This structural transformation resembles the polar rhombohedral phase observed in several other studies of  $\text{HfO}_2$ -based thin films. For example, Cheema *et al.* pointed out an increasingly rhombic distortion of the  $\text{Hf}_{1-x}\text{Zr}_x\text{O}_2$  polyhedra in their ferroelectric  $\text{Hf}_{0.8}\text{Zr}_{0.2}\text{O}_2$  thin films with decreasing thickness [2] and several studies specifically identified the  $R3$  and  $R3m$  phases as the rhombohedral polar phase [66,67]. Figure S7 in the SM [53] provides evidence of the structural resemblance of the asymmetric slab at a thickness of three Hf half layers to the bulk  $R3$  phase.

### C. $\text{Hf}_{0.5}\text{Zr}_{0.5}\text{O}_2$ and $\text{ZrO}_2$

As with the pure  $\text{HfO}_2$ , we first calculate the surface energies as we vary the composition of the orthorhombic  $\text{Hf}_{0.5}\text{Zr}_{0.5}\text{O}_2(001)$  surfaces, where the polarization is normal to the surface. We limited our calculations to O-terminated surfaces because in our prior study on

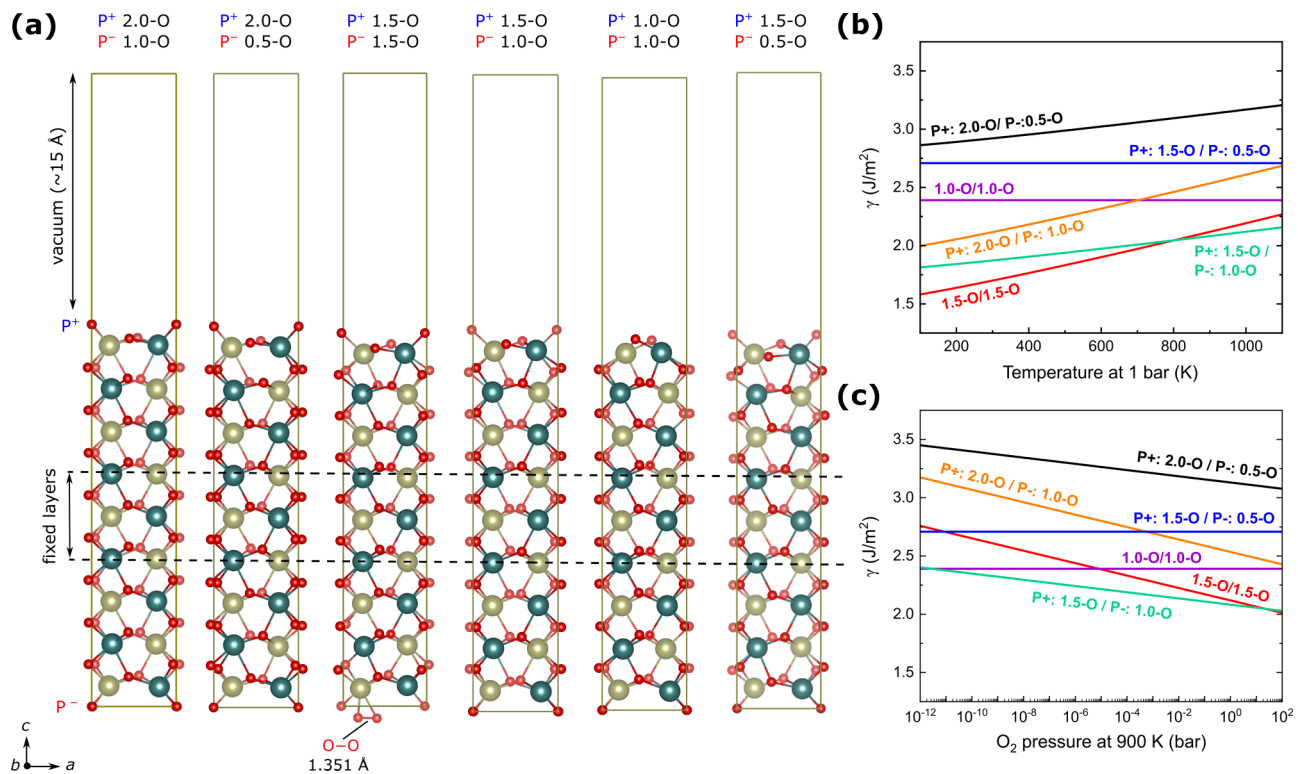


FIG. 3. (a) Profile views of the relaxed structures for orthorhombic  $\text{Hf}_{0.5}\text{Zr}_{0.5}\text{O}_2$  supercell slabs. The compositions of the outermost layers in terms of atoms per formula unit (p.f.u.) of the surface are labeled for the top and bottom layer above each structure (see Sec. III A and Fig. S1 [53] for the explanation of the nomenclature). The middle three Hf/Zr and two O half layers for all slabs are fixed to their bulklike arrangement with the polarization direction normal to the surface as labeled. The fainter atoms are farther away from the viewer. Plots of the surface energy as a function of (b) temperature from 100 to 1100 K at 1 bar  $\text{O}_2$  and (c) pressure from  $10^{-12}$  to  $10^2$  bar at 900 K corresponding to the slabs in (a).

orthorhombic  $\text{HfO}_2(001)$  surfaces we showed Hf-terminated surfaces (1.0-Hf and 0.5-Hf) to be energetically unstable due to the larger loss of coordination for the cation than for O if they were the terminal atoms [23]. Profile views of the slab models with varying O-terminated compositions are shown in Fig. 3(a).

Appendix B of the SM [53] presents the derivation of the thermodynamic expressions we used to calculate the surface free energies as a function of temperature and partial pressure of  $\text{O}_2$ .

The surface energies as a function of temperature and pressure are plotted in Figs. 3(b) and 3(c). We find that the surface energy landscape of orthorhombic  $\text{Hf}_{0.5}\text{Zr}_{0.5}\text{O}_2(001)$  surfaces is indeed similar to that of polar orthorhombic  $\text{HfO}_2(001)$  surfaces that we previously calculated [23]. At 1 bar, the most stable surface composition is the 1.5-O/1.5-O surface at low temperatures and the compositionally asymmetric  $\text{P}^+ : 1.5\text{-O} / \text{P}^- : 1.0\text{-O}$  at high temperatures. Although 1.5-O/1.5-O is compositionally symmetric, its  $\text{P}^+$  and  $\text{P}^-$  surfaces are structurally asymmetric not just because of the polarization displacements being opposite but because their respective terminal O atoms are in different oxidation states. The O atoms on the  $\text{P}^+$  surface are all closer to being bulklike oxide dianions whereas on the  $\text{P}^-$  surface, some of the terminal O atoms form a superoxidelike species, i.e., are oxidized [Fig. 3(a)]. This behavior is consistent with the ionic charge passivation mechanism, as we also noted and observed for

pure  $\text{HfO}_2$  in Ref. [23], where the  $\text{P}^+$  requires excess negative ions whereas the  $\text{P}^-$  requires reduced negative charge accumulation, hence the oxidation of the surface O atoms on  $\text{P}^-$ . The transition between 1.5-O/1.5-O and  $\text{P}^+ : 1.5\text{-O} / \text{P}^- : 1.0\text{-O}$  occurs at 800 K for  $\text{Hf}_{0.5}\text{Zr}_{0.5}\text{O}_2$  whereas it occurs at 680 K (at 1 bar) for  $\text{HfO}_2$  [23]. A further difference between the  $\text{Hf}_{0.5}\text{Zr}_{0.5}\text{O}_2(001)$  and  $\text{HfO}_2(001)$  surface energies is that they are lower by  $\sim 3\%$ – $6\%$  for  $\text{Hf}_{0.5}\text{Zr}_{0.5}\text{O}_2$  compared to  $\text{HfO}_2$  (calculated by comparing the lowest surface energies across the temperature range of 100–1100 K and 1 bar).

The surface energies calculated here for the ferroelectric orthorhombic phase of  $\text{Hf}_{0.5}\text{Zr}_{0.5}\text{O}_2$  are lower than those calculated by Materlik *et al.* [68]. For example, they report a calculated value of  $2.58 \text{ J/m}^2$  whereas we find the surface energy for the most stable surface composition to be  $2.12 \text{ J/m}^2$  at 900 K and 1 bar and to not exceed  $2.28 \text{ J/m}^2$  at the highest temperature range of 1100 K. In addition to conceptual difficulties with the phenomenological model used by Materlik *et al.* that have been pointed out by Park *et al.* [69], we can expect differences from our calculations reported here because they did not perform direct experimental measurements or obtain the values from first principles, but rather extrapolated from the experimental surface energies of nonpolar monoclinic and tetragonal phases of  $\text{HfO}_2$  and  $\text{ZrO}_2$  phases [68].

We next calculated the surface energies of orthorhombic  $\text{ZrO}_2(001)$  surfaces. In a similar fashion to  $\text{Hf}_{0.5}\text{Zr}_{0.5}\text{O}_2$ , the profile views of the slab models with varying O-terminated

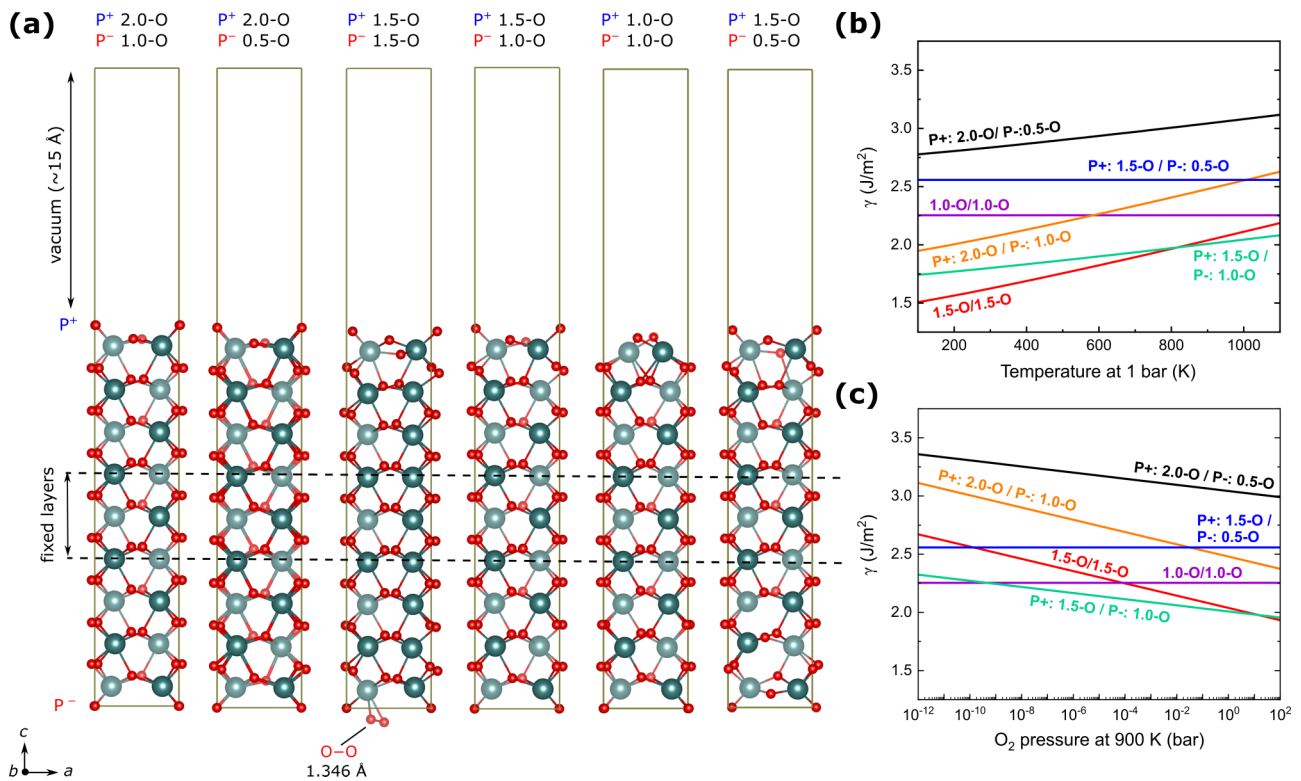


FIG. 4. (a) Profile views of the relaxed structures for orthorhombic  $\text{ZrO}_2$  supercell slabs. The composition of the outermost layers in terms of atoms p.f.u. of the surface is labeled for the top and bottom layer above each structure (see Sec. III A and Fig. S1 [53] for the explanation of the nomenclature). The middle three Zr and two O half layers for all slabs are fixed to their bulklike arrangement with the polarization direction normal to the surface as labeled. The fainter atoms are farther away from the viewer. Plots of the surface energy as a function of (b) temperature from 100 to 1100 K at 1 bar  $\text{O}_2$  and (c) pressure from  $10^{-12}$  to  $10^2$  bar at 900 K corresponding to the slabs in (a).

compositions are shown in Fig. 4(a) where the polarization is normal to the surface. The surface energies as a function of temperature and pressure are plotted in Figs. 4(b) and 4(c) (see again Appendix B of the SM [53] for the expression we used to calculate the surface energies). We find that the surface energy landscape of orthorhombic  $\text{ZrO}_2(001)$  surfaces is also similar to that of  $\text{HfO}_2(001)$  and  $\text{Hf}_{0.5}\text{Zr}_{0.5}\text{O}_2(001)$  where, at 1 bar, the most stable surface composition is the 1.5-O/1.5-O surface at low temperatures (also structurally asymmetric) and P+:1.5-O/P-:1.0-O at high temperatures. In this case, the transition between the two occurs at 820 K at 1 bar—higher than for the Hf-containing phases. The surface energies of  $\text{ZrO}_2$  are also lower by  $\sim 6\% - 10\%$  compared to  $\text{HfO}_2$  (again calculated by comparing the lowest surface energies across the temperature range of 100–1100 K and 1 bar). This follows a trend that the surface energies decrease slightly with increasing Zr content.

After establishing that  $\text{Hf}_{0.5}\text{Zr}_{0.5}\text{O}_2$  and  $\text{ZrO}_2$  slabs that are O rich at their positively polarized surface (P+:1.5-O/P-:1.0-O) correspond to the most stable surface composition at high temperatures and at 1 bar (as is also the case of pure  $\text{HfO}_2$ ), we next examined how the surface composition affects the stability of the polar orthorhombic phase and the magnitude of such polarization as a function of thickness for these Zr-containing phases.

Beginning with  $\text{Hf}_{0.5}\text{Zr}_{0.5}\text{O}_2$ , we plot the characteristic polar displacement of O atoms across  $\text{Hf}_{0.5}\text{Zr}_{0.5}\text{O}_2$  slabs of varying total thickness in Fig. 5(a), obtained in a similar

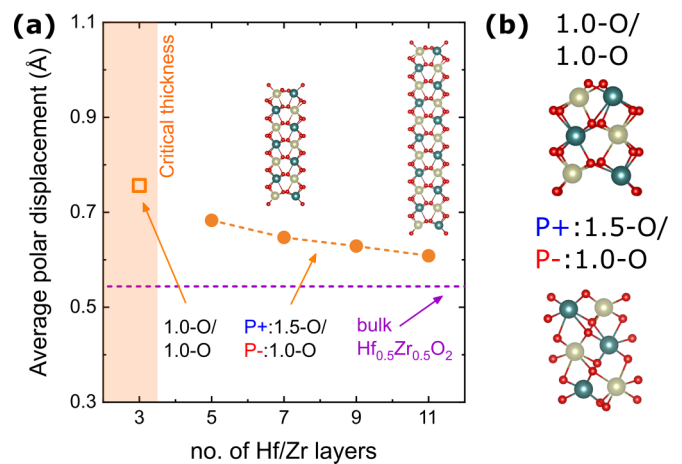


FIG. 5. (a) Average value of the polar displacements of O [see Fig. 1(a) for definition] for  $\text{Hf}_{0.5}\text{Zr}_{0.5}\text{O}_2$ . Dashed purple line provides a comparison to the bulk polar displacement. Inset figures show profile view of 11- and seven-layer-thick slabs (green spheres are Hf, dark cyan spheres are Zr, and red spheres are O). At three layers (labeled “critical thickness”) the asymmetric  $\text{Hf}_{0.5}\text{Zr}_{0.5}\text{O}_2$  structure [shown in bottom panel (b)] deviates significantly from the bulk orthorhombic phase. Thus, as for the case of  $\text{HfO}_2$ , we do not plot its average O displacement. In its place, the average polar displacement is plotted for the symmetric slab [top panel (b)]. (b) Three-layer optimized structures for the symmetric (top panel) and asymmetric (bottom panel)  $\text{Hf}_{0.5}\text{Zr}_{0.5}\text{O}_2$  slab structures.

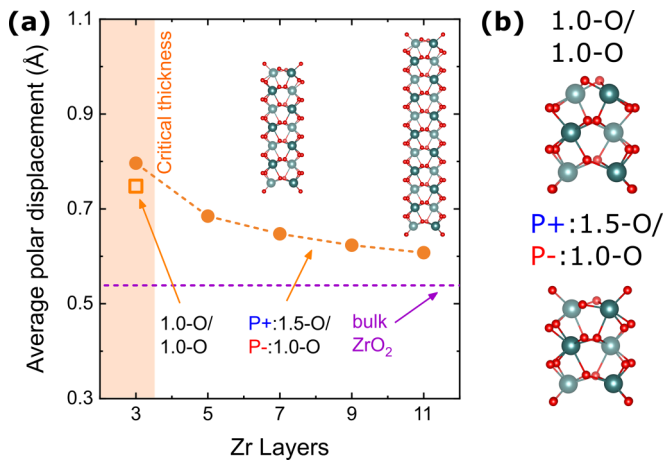


FIG. 6. (a) Average value of the polar displacements of O [see Fig. 1(a) for definition] for  $\text{ZrO}_2$ . Dashed purple line provides a comparison to the bulk polar displacement. Inset figures show profile view of 11- and seven-layer-thick slabs (green spheres are Zr and red spheres are O). (b) Three-layer optimized structures for the symmetric (top panel) and asymmetric (bottom panel)  $\text{ZrO}_2$  slab structures.

fashion to the case of  $\text{HfO}_2$  plotted in Fig. 2(a). Trends found in  $\text{HfO}_2$  are also found for  $\text{Hf}_{0.5}\text{Zr}_{0.5}\text{O}_2$ . The average polar displacements at 11-layer thickness for an asymmetric P+:1.5-O/P-:1.0-O slab have a stable polarization larger than the bulk that increases with decreasing thickness ( $\sim 11.8\%$  at 11-layer thickness to  $\sim 25.6\%$  at five-layer thickness). At three-layer thickness, as for  $\text{HfO}_2$ , we find that an asymmetric  $\text{Hf}_{0.5}\text{Zr}_{0.5}\text{O}_2$  slab also undergoes a transition to a rhombohedral-like structure, and polarization for a symmetric 1.0-O/1.0-O-terminated stoichiometric  $\text{Hf}_{0.5}\text{Zr}_{0.5}\text{O}_2$  slab is also stable and retains its structural resemblance to the bulk orthorhombic phase [Fig. 5(b)].

Likewise, we also plot the characteristic polar displacement of O across pure  $\text{ZrO}_2$  slabs of varying total thickness in Fig. 6(a), obtained in a similar fashion to the prior cases of  $\text{HfO}_2$  and  $\text{Hf}_{0.5}\text{Zr}_{0.5}\text{O}_2$ . Trends similar to those of  $\text{HfO}_2$  and  $\text{Hf}_{0.5}\text{Zr}_{0.5}\text{O}_2$  are found for  $\text{ZrO}_2$ . The average polar displacements at 11-layer thickness for an asymmetric P+:1.5-O/P-:1.0-O slab results in a stable polarization larger than the bulk that increases with decreasing thickness ( $\sim 12.8\%$  at 11-layer thickness to  $\sim 27.1\%$  at five-layer thickness). However, one difference is that at three-layer thickness, we find that the asymmetric  $\text{ZrO}_2$  slab does not undergo a phase transition and instead both asymmetric and symmetric  $\text{ZrO}_2$  retain their orthorhombic-like structure [Fig. 5(b)]. Therefore, unlike for the other two materials, we plot our prediction for the asymmetric three-layer case in Fig. 6(a). We also confirm that, due to the greater ionic charge screening, this average polar displacement value for the three-layer asymmetric  $\text{ZrO}_2$  slab ( $\sim 48\%$ ) is larger than the corresponding displacement ( $\sim 39\%$ ) in the three-layer symmetric  $\text{ZrO}_2$  slab.

Although ferroelectric  $\text{HfO}_2$ -based thin films down to  $\sim 1$  nm thickness have been experimentally demonstrated [2,70], there is variation in experimental reports where the polarization may increase with decreasing thickness only to a certain point before decreasing or vanishing entirely, especially below 5 nm [42,43,71–73]. Given the variation in experimental

reports of the ferroelectric polarization and performance with decreasing thickness, here we emphasize the role that the surface or interface composition can play at the nanoscale to stabilize the polarization phase. For example, further complexity is introduced by the presence of the electrodes. Their work functions may affect screening the electrostatic potential and the chemical reactivity of the interface with the electrode may lead to formation of an interfacial layer that can degrade performance.

Furthermore, because we fixed the in-plane lattice constant to the bulk orthorhombic value, the stabilization of the orthorhombic phase via an asymmetric construction that is O rich at the P+ surface is not necessarily the only perturbation leading to thermodynamically favoring the orthorhombic phase over the monoclinic phase at the nanoscale for  $\text{HfO}_2$ ,  $\text{Hf}_{0.5}\text{Zr}_{0.5}\text{O}_2$ , or  $\text{ZrO}_2$ . Rather, a combination of in-plane strain and compositional modification can stabilize the polar orthorhombic over the nonpolar monoclinic phase. Indeed, a monoclinic slab is still lower in energy than an orthorhombic slab regardless of the surface composition. This is consistent with the current understanding of the epitaxial stabilization of the orthorhombic phase (e.g., see Park *et al.* [69] and Schroeder *et al.* [74]) where it is the suppression of the transition to the nonpolar monoclinic phase through the optimal engineering of the synthesis and fabrication of  $\text{HfO}_2$ -based thin films that can achieve the stabilization of the polar phases.

We end by further examining one of the trends in the relative stability of polar phases across the composition of  $\text{Hf}_x\text{Zr}_{1-x}\text{O}_2$ . While the surface energy of polar orthorhombic slabs in this work decreases with increasing Zr content ( $\sim 6\%–10\%$  lower for  $\text{ZrO}_2$  than  $\text{HfO}_2$ ), we should not expect the polar orthorhombic phase of  $\text{ZrO}_2$  thin films to be more stable than  $\text{HfO}_2$  or  $\text{ZrO}_2$ . This is because the bulk nonpolar tetragonal phase of  $\text{ZrO}_2$  makes a larger gain in relative stability than the bulk orthorhombic phase compared to the case of  $\text{HfO}_2$ , although neither are lower than their respective monoclinic phase. Specifically, while the enthalpy difference (at 0 K) between the transition from  $o\text{-ZrO}_2 \rightarrow m\text{-ZrO}_2$  is  $\sim 94\%$  higher than the transition from  $o\text{-HfO}_2 \rightarrow m\text{-HfO}_2$ , the transition enthalpy for  $t\text{-ZrO}_2 \rightarrow m\text{-ZrO}_2$  is only  $\sim 54\%$  higher than that of  $t\text{-HfO}_2 \rightarrow m\text{-HfO}_2$  (see Fig. S8 in the SM [53]). Indeed, this has been previously pointed out as a contributing factor to the antiferroelectric (arising from the tetragonal phase) behavior that is typical of  $\text{ZrO}_2$  thin films [45,75]. Instead, this work serves to describe contributing factors to the more recent reports of stable polar orthorhombic  $\text{ZrO}_2$  thin films [44] that have not been previously explored, i.e., that a net electrostatic potential that decreases with thickness can also be more adequately screened at small scales with additional control of interface composition.

#### IV. SUMMARY AND OUTLOOK

We find that surface composition plays a critical role in the ferroelectric stability of orthorhombic  $\text{Hf}_x\text{Zr}_{1-x}\text{O}_2$  thin films, which can enable stable polarization without a critical thickness limit under an open-circuit boundary condition and epitaxial constraint. At 11-layer thicknesses, surface polarization for stoichiometric orthorhombic  $\text{HfO}_2$ ,

Hf<sub>0.5</sub>Zr<sub>0.5</sub>O<sub>2</sub>, and ZrO<sub>2</sub> slabs with a symmetric surface composition (1.0-O/1.0-O) is unstable and they depolarize to a nonpolar monoclinic phase. In contrast, nonstoichiometric slabs with an O-rich positively polarized surface composition (P+:1.5-O/P-:1.0-O) can retain bulklike ferroelectric displacements.

We also find that the polarization increases as the thickness decreases for nonstoichiometric slabs, as calculated by the average structural polar displacements, with five-layer-thick slabs achieving a larger polarization than the bulk for HfO<sub>2</sub>, Hf<sub>0.5</sub>Zr<sub>0.5</sub>O<sub>2</sub>, and ZrO<sub>2</sub>. Additionally, at a critical thickness of three layers, we predict that symmetric stoichiometric HfO<sub>2</sub> and Hf<sub>0.5</sub>Zr<sub>0.5</sub>O<sub>2</sub> slabs can sustain an unscreened ferroelectric polarization with a stable bulklike orthorhombic phase while the asymmetric nonstoichiometric slabs undergo a phase transition to a polar rhombohedral *R3*-like phase.

The evolution of the polarization and polar distortions with decreasing thickness found here is consistent with recent experimentally reported behavior of ferroelectricity in

Hf<sub>x</sub>Zr<sub>1-x</sub>O<sub>2</sub> thin films [2,44]. These results highlight the importance of the surface composition which plays a determinative role at ultrathin thickness limits. Control of the surface composition is a critical mechanism for optimizing the ferroelectric performance of Hf<sub>x</sub>Zr<sub>1-x</sub>O<sub>2</sub> thin films toward next generation nanoscale applications, e.g., ferroelectric memory and logic devices.

#### ACKNOWLEDGMENTS

J.P.C. and A.A. acknowledge support from the National Science Foundation (NSF) through Cooperative Agreement Award No. EEC-1160504 for Solicitation No. NSF 11-537 (TANMS). E.A.C. acknowledges financial support from the University of California, Los Angeles for this project. This paper used computational and storage services associated with the Hoffman2 Shared Cluster provided by the UCLA Institute for Digital Research and Education's Research Technology Group.

- 
- [1] T. Böscke, J. Müller, D. Bräuhaus, U. Schröder, and U. Böttger, Ferroelectricity in hafnium oxide thin films, *Appl. Phys. Lett.* **99**, 102903 (2011).
- [2] S. S. Cheema, D. Kwon, N. Shanker, R. Dos Reis, S.-L. Hsu, J. Xiao, H. Zhang, R. Wagner, A. Datar, M. R. McCarter *et al.*, Enhanced ferroelectricity in ultrathin films grown directly on silicon, *Nature (London)* **580**, 478 (2020).
- [3] H.-J. Lee, M. Lee, K. Lee, J. Jo, H. Yang, Y. Kim, S. C. Chae, U. Waghmare, and J. H. Lee, Scale-free ferroelectricity induced by flat phonon bands in HfO<sub>2</sub>, *Science* **369**, 1343 (2020).
- [4] J. Lyu, T. Song, I. Fina, and F. Sánchez, High polarization, endurance and retention in sub-5 nm Hf<sub>0.5</sub>Zr<sub>0.5</sub>O<sub>2</sub> films, *Nanoscale* **12**, 11280 (2020).
- [5] F. Delodovici, P. Barone, and S. Picozzi, Trilinear-coupling-driven ferroelectricity in HfO<sub>2</sub>, *Phys. Rev. Mater.* **5**, 064405 (2021).
- [6] T. Mikolajick, S. Slesazeck, M. H. Park, and U. Schroeder, Ferroelectric hafnium oxide for ferroelectric random-access memories and ferroelectric field-effect transistors, *MRS Bull.* **43**, 340 (2018).
- [7] J. Müller, T. S. Böscke, S. Müller, E. Yurchuk, P. Polakowski, J. Paul, D. Martin, T. Schenk, K. Khullar, A. Kersch *et al.*, Ferroelectric hafnium oxide: A CMOS-compatible and highly scalable approach to future ferroelectric memories, in *Proceedings of the 2013 IEEE International Electron Devices Meeting* (IEEE, New York, 2013), pp. 10.8.1–10.8.4.
- [8] M. H. Park, Y. H. Lee, T. Mikolajick, U. Schroeder, and C. S. Hwang, Review and perspective on ferroelectric HfO<sub>2</sub>-based thin films for memory applications, *MRS Commun.* **8**, 795 (2018).
- [9] B. Prasad, V. Thakare, A. Kalitsov, Z. Zhang, B. Terris, and R. Ramesh, Large tunnel electroresistance with ultrathin Hf<sub>0.5</sub>Zr<sub>0.5</sub>O<sub>2</sub> ferroelectric tunnel barriers, *Adv. Electron. Mater.* **7**, 2001074 (2021).
- [10] D. G. Schlom, S. Guha, and S. Datta, Gate oxides beyond SiO<sub>2</sub>, *MRS Bull.* **33**, 1017 (2008).
- [11] D. G. Schlom and J. H. Haeni, A thermodynamic approach to selecting alternative gate dielectrics, *MRS Bull.* **27**, 198 (2002).
- [12] C. Dubourdieu, J. Bruley, T. M. Arruda, A. Posadas, J. Jordan-Sweet, M. M. Frank, E. Cartier, D. J. Frank, S. V. Kalinin, A. A. Demkov *et al.*, Switching of ferroelectric polarization in epitaxial BaTiO<sub>3</sub> films on silicon without a conducting bottom electrode, *Nat. Nanotechnol.* **8**, 748 (2013).
- [13] M. P. Warusawithana, C. Cen, C. R. Slesman, J. C. Woicik, Y. Li, L. F. Kourkoutis, J. A. Klug, H. Li, P. Ryan, L.-P. Wang *et al.*, A ferroelectric oxide made directly on silicon, *Science* **324**, 367 (2009).
- [14] K. Z. Rushchanskii, S. Blügel, and M. Ležaić, Ordering of oxygen vacancies and related ferroelectric properties in HfO<sub>2-δ</sub>, *Phys. Rev. Lett.* **127**, 087602 (2021).
- [15] Y. Qi and K. M. Rabe, Phase competition in HfO<sub>2</sub> with applied electric field from first principles, *Phys. Rev. B* **102**, 214108 (2020).
- [16] R. Batra, T. D. Huan, J. L. Jones, G. Rossetti Jr., and R. Ramprasad, Factors favoring ferroelectricity in hafnia: A first-principles computational study, *J. Phys. Chem. C* **121**, 4139 (2017).
- [17] R. Batra, T. D. Huan, G. A. Rossetti Jr., and R. Ramprasad, Dopants promoting ferroelectricity in hafnia: Insights from a comprehensive chemical space exploration, *Chem. Mater.* **29**, 9102 (2017).
- [18] S. V. Levchenko and A. M. Rappe, Influence of ferroelectric polarization on the equilibrium stoichiometry of lithium niobate (0001) surfaces, *Phys. Rev. Lett.* **100**, 256101 (2008).
- [19] X. Xu, F.-T. Huang, Y. Qi, S. Singh, K. M. Rabe, D. Obeysekera, J. Yang, M.-W. Chu, and S.-W. Cheong, Kinetically stabilized ferroelectricity in bulk single-crystalline HfO<sub>2</sub>:Y, *Nat. Mater.* **20**, 826 (2021).
- [20] R. V. Wang, D. D. Fong, F. Jiang, M. J. Highland, P. H. Fuoss, C. Thompson, A. M. Kolpak, J. A. Eastman, S. K. Streiffer, A. M. Rappe, and G. B. Stephenson, Reversible chemical switching of a ferroelectric film, *Phys. Rev. Lett.* **102**, 047601 (2009).

- [21] N. A. Spaldin, I. Efe, M. D. Rossell, and C. Gattinoni, Layer and spontaneous polarizations in perovskite oxides and their interplay in multiferroic bismuth ferrite, *J. Chem. Phys.* **154**, 154702 (2021).
- [22] W. A. Saidi, J. M. P. Martirez, and A. M. Rappe, Strong reciprocal interaction between polarization and surface stoichiometry in oxide ferroelectrics, *Nano Lett.* **14**, 6711 (2014).
- [23] A. Acosta, J. M. P. Martirez, N. Lim, J. P. Chang, and E. A. Carter, Relationship between ferroelectric polarization and stoichiometry of  $\text{HfO}_2$  surfaces, *Phys. Rev. Mater.* **5**, 124417 (2021).
- [24] S. Estandía, J. Gàzquez, M. Varela, N. Dix, M. Qian, R. Solanas, I. Fina, and F. Sánchez, Critical effect of the bottom electrode on the ferroelectricity of epitaxial  $\text{Hf}_{0.5}\text{Zr}_{0.5}\text{O}_2$  thin films, *J. Mater. Chem. C* **9**, 3486 (2021).
- [25] W. Hamouda, A. Pancotti, C. Lubin, L. Tortech, C. Richter, T. Mikolajick, U. Schroeder, and N. Barrett, Physical chemistry of the  $\text{TiN}/\text{Hf}_{0.5}\text{Zr}_{0.5}\text{O}_2$  interface, *J. Appl. Phys.* **127**, 064105 (2020).
- [26] P. D. Lomenzo, Q. Takmeel, C. Zhou, C. M. Fancher, E. Lambers, N. G. Rudawski, J. L. Jones, S. Moghaddam, and T. Nishida, TaN interface properties and electric field cycling effects on ferroelectric Si-doped  $\text{HfO}_2$  thin films, *J. Appl. Phys.* **117**, 134105 (2015).
- [27] M. H. Park, H. J. Kim, Y. J. Kim, W. Jeon, T. Moon, and C. S. Hwang, Ferroelectric properties and switching endurance of  $\text{Hf}_{0.5}\text{Zr}_{0.5}\text{O}_2$  films on TiN bottom and TiN or  $\text{RuO}_2$  top electrodes, *Phys. Status Solidi RRL* **8**, 532 (2014).
- [28] S. S. Fields, S. W. Smith, C. M. Fancher, M. D. Henry, S. L. Wolfley, M. G. Sales, S. T. Jaszewski, M. A. Rodriguez, G. Esteves, P. S. Davids *et al.*, Metal nitride electrode stress and chemistry effects on phase and polarization response in ferroelectric  $\text{Hf}_{0.5}\text{Zr}_{0.5}\text{O}_2$  thin films, *Adv. Mater. Interfaces* **8**, 2100018 (2021).
- [29] T. Szyjka, L. Baumgarten, T. Mittmann, Y. Matveyev, C. Schlueter, T. Mikolajick, U. Schroeder, and M. Müller, Enhanced ferroelectric polarization in  $\text{TiN}/\text{HfO}_2/\text{TiN}$  capacitors by interface design, *ACS Appl. Electron. Mater.* **2**, 3152 (2020).
- [30] R. Athle, A. E. Persson, A. Irish, H. Menon, R. Timm, and M. Borg, Effects of TiN top electrode texturing on ferroelectricity in  $\text{Hf}_{1-x}\text{Zr}_x\text{O}_2$ , *ACS Appl. Mater. Interfaces* **13**, 11089 (2021).
- [31] M. Yadav, A. Kashir, S. Oh, R. D. Nikam, H. Kim, H. Jang, and H. Hwang, High polarization and wake-up free ferroelectric characteristics in ultrathin  $\text{Hf}_{0.5}\text{Zr}_{0.5}\text{O}_2$  devices by control of oxygen-deficient layer, *Nanotechnology* **33**, 085206 (2021).
- [32] T. Szyjka, L. Baumgarten, T. Mittmann, Y. Matveyev, C. Schlueter, T. Mikolajick, U. Schroeder, and M. Müller, Chemical stability of  $\text{IrO}_2$  top electrodes in ferroelectric  $\text{Hf}_{0.5}\text{Zr}_{0.5}\text{O}_2$ -based metal-insulator-metal structures: The impact of annealing gas, *Phys. Status Solidi RRL* **15**, 2100027 (2021).
- [33] T. Mittmann, T. Szyjka, H. Alex, M. C. Istrate, P. D. Lomenzo, L. Baumgarten, M. Müller, J. L. Jones, L. Pintilie, T. Mikolajick *et al.*, Impact of iridium oxide electrodes on the ferroelectric phase of thin  $\text{Hf}_{0.5}\text{Zr}_{0.5}\text{O}_2$  films, *Phys. Status Solidi RRL* **15**, 2100012 (2021).
- [34] P. Jiang, Q. Luo, X. Xu, T. Gong, P. Yuan, Y. Wang, Z. Gao, W. Wei, L. Tai, and H. Lv, Wake-up effect in  $\text{HfO}_2$ -based ferroelectric films, *Adv. Electron. Mater.* **7**, 2000728 (2021).
- [35] M. Hoffmann, U. Schroeder, T. Schenk, T. Shimizu, H. Funakubo, O. Sakata, D. Pohl, M. Drescher, C. Adelman, R. Materlik *et al.*, Stabilizing the ferroelectric phase in doped hafnium oxide, *J. Appl. Phys.* **118**, 072006 (2015).
- [36] A. G. Chernikova, M. G. Kozodaev, R. R. Khakimov, S. N. Polyakov, and A. Markeev, Influence of ALD Ru bottom electrode on ferroelectric properties of  $\text{Hf}_{0.5}\text{Zr}_{0.5}\text{O}_2$ -based capacitors, *Appl. Phys. Lett.* **117**, 192902 (2020).
- [37] K. P. Kelley, A. N. Morozovska, E. A. Eliseev, Y. Liu, S. S. Fields, S. T. Jaszewski, T. Mimura, S. Calderon, E. C. Dickey, J. F. Ihlefeld *et al.*, Ferroelectricity in hafnia controlled via surface electrochemical state, *Nat. Mater.* **22**, 1144 (2023).
- [38] R. Batra, H. D. Tran, and R. Ramprasad, Stabilization of metastable phases in hafnia owing to surface energy effects, *Appl. Phys. Lett.* **108**, 172902 (2016).
- [39] J. Muller, T. S. Boscke, U. Schroeder, S. Mueller, D. Brauhaus, U. Bottger, L. Frey, and T. Mikolajick, Ferroelectricity in simple binary  $\text{ZrO}_2$  and  $\text{HfO}_2$ , *Nano Lett.* **12**, 4318 (2012).
- [40] S. Shibayama, T. Nishimura, S. Migita, and A. Toriumi, Thermodynamic control of ferroelectric-phase formation in  $\text{Hf}_x\text{Zr}_{1-x}\text{O}_2$  and  $\text{ZrO}_2$ , *J. Appl. Phys.* **124**, 184101 (2018).
- [41] M. H. Park, H. J. Kim, Y. J. Kim, Y. H. Lee, T. Moon, K. D. Kim, S. D. Hyun, F. Fengler, U. Schroeder, C. S. Hwang *et al.*, Effect of Zr content on the wake-up effect in  $\text{Hf}_{1-x}\text{Zr}_x\text{O}_2$  films, *ACS Appl. Mater. Interfaces* **8**, 15466 (2016).
- [42] J. Cao, S. Shi, Y. Zhu, and J. Chen, An overview of ferroelectric hafnia and epitaxial growth, *Phys. Status Solidi RRL* **15**, 2100025 (2021).
- [43] S. Migita, H. Ota, H. Yamada, K. Shibuya, A. Sawa, and A. Toriumi, Polarization switching behavior of Hf-Zr-O ferroelectric ultrathin films studied through coercive field characteristics, *Jpn. J. Appl. Phys.* **57**, 04FB01 (2018).
- [44] S. S. Cheema, N. Shanker, S.-L. Hsu, Y. Rho, C.-H. Hsu, V. A. Stoica, Z. Zhang, J. W. Freeland, P. Shafer, C. P. Grigoropoulos *et al.*, Emergent ferroelectricity in subnanometer binary oxide films on silicon, *Science* **376**, 648 (2022).
- [45] A. Christensen and E. A. Carter, First-principles study of the surfaces of zirconia, *Phys. Rev. B* **58**, 8050 (1998).
- [46] V. Lenzi, J. P. Silva, B. Šmíd, V. Matolín, C. M. Istrate, C. Ghica, J. L. MacManus-Driscoll, and L. Marques, Ferroelectricity induced by oxygen vacancies in rhombohedral  $\text{ZrO}_2$  thin films, *Energy Environ. Mater.* (2022) doi: 10.1002/eem2.12500.
- [47] A. El Boutaybi, T. Maroutian, L. Largeau, S. Matzen, and P. Lecoer, Stabilization of the epitaxial rhombohedral ferroelectric phase in  $\text{ZrO}_2$  by surface energy, *Phys. Rev. Mater.* **6**, 074406 (2022).
- [48] J. P. Silva, R. F. Negrea, M. C. Istrate, S. Dutta, H. Aramberri, J. Íñiguez, F. G. Figueiras, C. Ghica, K. C. Sekhar, and A. L. Kholkin, Wake-up free ferroelectric rhombohedral phase in epitaxially strained  $\text{ZrO}_2$  thin films, *ACS Appl. Mater. Interfaces* **13**, 51383 (2021).
- [49] G. Kresse and J. Furthmüller, Efficient iterative schemes for *ab initio* total-energy calculations using a plane-wave basis set, *Phys. Rev. B* **54**, 11169 (1996).
- [50] J. P. Perdew, K. Burke, and M. Ernzerhof, Generalized gradient approximation made simple, *Phys. Rev. Lett.* **77**, 3865 (1996).
- [51] P. E. Blöchl, Projector augmented-wave method, *Phys. Rev. B* **50**, 17953 (1994).
- [52] H. J. Monkhorst and J. D. Pack, Special points for Brillouin-zone integrations, *Phys. Rev. B* **13**, 5188 (1976).

- [53] See Supplemental Material at <http://link.aps.org/supplemental/10.1103/PhysRevMaterials.7.124401> for further explanation of the nomenclature used to describe the slab surface compositions, additional structural characterization and comparison of the symmetrically and asymmetrically terminated 11 Hf layer thick HfO<sub>2</sub> slabs to the bulk monoclinic or orthorhombic phases; layer-by-layer pDOS of the symmetrically and asymmetrically terminated 11 Hf layer thick HfO<sub>2</sub> slabs; the layer-by-layer O-planar-displacement profiles for the asymmetrically terminated polar HfO<sub>2</sub> slabs with five to 11 Hf layers; plane-averaged electrostatic potential profiles of HfO<sub>2</sub> for the symmetrically and asymmetrically terminated HfO<sub>2</sub> slabs with three to 11 Hf layers; layer-by-layer pDOS of the unrelaxed and relaxed symmetrically terminated three Hf layer thick HfO<sub>2</sub> slabs; profile view and comparison of the rhombohedral R3 HfO<sub>2</sub> phase to the three Hf layer thick asymmetrically terminated HfO<sub>2</sub> slab; enthalpies of the orthorhombic and tetragonal phases relative to the monoclinic phase for bulk HfO<sub>2</sub>, Hf<sub>0.5</sub>Zr<sub>0.5</sub>O<sub>2</sub>, and ZrO<sub>2</sub>; comparison of the experimental lattice parameters to those computed in this work; and derivation of the Hf<sub>0.5</sub>Zr<sub>0.5</sub>O<sub>2</sub> and ZrO<sub>2</sub> surface free energy expressions.
- [54] R. Ruh, and P. W. R. Corfield, Crystal structure of monoclinic hafnia and comparison with monoclinic zirconia, *J. Am. Ceram. Soc.* **53**, 126 (1970).
- [55] A. Togo and I. Tanaka, First principles phonon calculations in materials science, *Scr. Mater.* **108**, 1 (2015).
- [56] J. P. Perdew, A. Ruzsinszky, G. I. Csonka, O. A. Vydrov, G. E. Scuseria, L. A. Constantin, X. Zhou, and K. Burke, Restoring the density-gradient expansion for exchange in solids and surfaces, *Phys. Rev. Lett.* **100**, 136406 (2008).
- [57] K. Momma and F. Izumi, VESTA 3 for three-dimensional visualization of crystal, volumetric and morphology data, *J. Appl. Crystallogr.* **44**, 1272 (2011).
- [58] V. Wang, N. Xu, J.-C. Liu, G. Tang, and W.-T. Geng, VASPKIT: A user-friendly interface facilitating high-throughput computing and analysis using VASP code, *Comput. Phys. Commun.* **267**, 108033 (2021).
- [59] T. D. Huan, V. Sharma, G. A. Rossetti, Jr., and R. Ramprasad, Pathways towards ferroelectricity in hafnia, *Phys. Rev. B* **90**, 064111 (2014).
- [60] J. Goniakowski, C. Noguera, and L. Giordano, Prediction of uncompensated polarity in ultrathin films, *Phys. Rev. Lett.* **98**, 205701 (2007).
- [61] C. Noguera and J. Goniakowski, Polarity in oxide ultrathin films, *J. Phys.: Condens. Matter* **20**, 264003 (2008).
- [62] H. Yu, M. Li, B. J. Cho, C. Yeo, M. Joo, D.-L. Kwong, J. Pan, C. Ang, J. Zheng, and S. Ramanathan, Energy gap and band alignment for (HfO<sub>2</sub>)<sub>x</sub>(Al<sub>2</sub>O<sub>3</sub>)<sub>1-x</sub> on (100) Si, *Appl. Phys. Lett.* **81**, 376 (2002).
- [63] W. Zhu, T. Tamagawa, M. Gibson, T. Furukawa, and T. Ma, Effect of Al inclusion in HfO<sub>2</sub> on the physical and electrical properties of the dielectrics, *IEEE Trans. Electron Devices* **23**, 649 (2002).
- [64] N. V. Nguyen, S. Sayan, I. Levin, J. R. Ehrstein, I. J. R. Baumvol, C. Driemeier, C. Krug, L. Wielunski, P. Y. Hung, and A. Diebold, Optical band gaps and composition dependence of hafnium–aluminate thin films grown by atomic layer chemical vapor deposition, *J. Vac. Sci. Technol.* **23**, 1706 (2005).
- [65] M. Modreanu, P. Hurley, B. O’Sullivan, B. O’Looney, J.-P. Senateur, H. Rousell, F. Rousell, M. Audier, C. Dubourdieu, I. W. Boyd *et al.*, in *Opto-Ireland 2002: Optics and Photonics Technologies and Applications* (International Society for Optics and Photonics, Bellingham, WA, 2003), p. 1236.
- [66] Y. Wei, P. Nukala, M. Salverda, S. Matzen, H. J. Zhao, J. Momand, A. S. Everhardt, G. Agnus, G. R. Blake, P. Lecoer *et al.*, A rhombohedral ferroelectric phase in epitaxially strained Hf<sub>0.5</sub>Zr<sub>0.5</sub>O<sub>2</sub> thin films, *Nat. Mater.* **17**, 1095 (2018).
- [67] P. Nukala, Y. Wei, V. de Haas, Q. Guo, J. Antoja-Lleonart, and B. Noheda, Guidelines for the stabilization of a polar rhombohedral phase in epitaxial Hf<sub>0.5</sub>Zr<sub>0.5</sub>O<sub>2</sub> thin films, *Ferroelectrics* **569**, 148 (2020).
- [68] R. Materlik, C. Künneth, and A. Kersch, The origin of ferroelectricity in Hf<sub>1-x</sub>Zr<sub>x</sub>O<sub>2</sub>: A computational investigation and a surface energy model, *J. Appl. Phys.* **117**, 134109 (2015).
- [69] M. H. Park, Y. H. Lee, T. Mikolajick, U. Schroeder, and C. S. Hwang, Thermodynamic and kinetic origins of ferroelectricity in fluorite structure oxides, *Adv. Electron. Mater.* **5**, 1800522 (2019).
- [70] S. S. Cheema, N. Shanker, C. H. Hsu, A. Datar, J. Bae, D. Kwon, and S. Salahuddin, One nanometer HfO<sub>2</sub>-based ferroelectric tunnel junctions on silicon, *Adv. Electron. Mater.* **8**, 2100499 (2021).
- [71] X. Tian, S. Shibayama, T. Nishimura, T. Yajima, S. Migita, and A. Toriumi, Evolution of ferroelectric HfO<sub>2</sub> in ultrathin region down to 3 nm, *Appl. Phys. Lett.* **112**, 102902 (2018).
- [72] X. Lyu, M. Si, X. Sun, M. Capano, H. Wang, and P. Ye, in *2019 Symposium on VLSI Technology* (IEEE, New York, 2019), p. T44.
- [73] M. H. Park, H. J. Kim, Y. J. Kim, W. Lee, T. Moon, and C. S. Hwang, Evolution of phases and ferroelectric properties of thin Hf<sub>0.5</sub>Zr<sub>0.5</sub>O<sub>2</sub> films according to the thickness and annealing temperature, *Appl. Phys. Lett.* **102**, 242905 (2013).
- [74] U. Schroeder, M. H. Park, T. Mikolajick, and C. S. Hwang, The fundamentals and applications of ferroelectric HfO<sub>2</sub>, *Nat. Rev. Mater.* **7**, 653 (2022).
- [75] M. Dogan, N. Gong, T.-P. Ma, and S. Ismail-Beigi, Causes of ferroelectricity in HfO<sub>2</sub>-based thin films: An *ab initio* perspective, *Phys. Chem. Chem. Phys.* **21**, 12150 (2019).